Ultramicroscopy 136 (2014) 86–90

Contents lists available at ScienceDirect

Ultramicroscopy

journal homepage: www.elsevier.com/locate/ultramic

Correction of nonlinear lateral distortions of scanning probe microscopy images

M. Schnedler, P.H. Weidlich, V. Portz, D. Weber, R.E. Dunin-Borkowski, Ph. Ebert *

Peter Grünberg Institut, Forschungszentrum Jülich GmbH, 52425 Jülich, Germany

ARTICLE INFO

Article history:
Received 12 June 2013
Received in revised form
1 August 2013
Accepted 8 August 2013
Available online 19 August 2013

Keywords:
Scanning probe microscopy
Image distortions
Correction algorithm
Calibration

ABSTRACT

A methodology for the correction of scanning probe microscopy image distortions is demonstrated. It is based on the determination of displacement vectors from the measurement of a calibration sample. By moving the pixels of the distorted scanning probe microscopy image along the displacement vectors an almost complete correction of the nonlinear, time independent distortions is achieved.

© 2013 Elsevier B.V. All rights reserved.

1. Introduction

The inverse piezoelectric effect is commonly utilized to position the tip or the cantilever with atomic precision in scanning probe microscopes (SPMs) [1]. Although the properties of modern piezoelectric materials are well known, their application in SPMs requires a calibration of their lateral and vertical positioning, which is usually achieved by acquiring images of atomic lattices and comparing them with the perfect periodical arrangement of the atoms of a crystalline surface. Hence, the calibration is optimized for a nanometer scan range. However, sometimes the measurement requires scanning parameters that exceed the designated linear range of the calibration. Then, nonlinear effects of the piezoceramic actuators, like hysteresis creep, drift, and a nonlinear dependence of the displacement on the applied voltage often result in image distortions. These effects are inherently connected with most scanning tubes [2] used in modern SPMs.

In order to overcome nonlinear piezoelectric effects, various attempts have been made. Most of them follow two different strategies: on the one hand, the different nonlinear effects of the piezoceramic are described theoretically, for example using a Preisach model [3]. Based on such a model, nonlinearities can be corrected while or after measurement. However, it is very difficult to include all types of nonlinearities in the model. On the other hand, optical [4–9] and capacitive [10,11] tracking systems (or a combination of both [12]) are used to determine the displacement of the piezoceramic during the actual scanning and data acquisition process. These tracking systems allow the acquisition of SPM images with high accuracy, but as a drawback, additional equipment within the scanning probe microscope is needed. Hence, it is very difficult to install such systems in existing SPMs.

A totally different approach applies a Fourier transform on distorted atomic scale images [13]. Due to the periodicity of the atomic lattice, distortions can be identified and corrected in the Fourier space. This method, commonly used in transmission electron microscopy, is only applicable for relatively small distortions.

In this paper we present a simple and fast method for correcting nonlinear, but reproducible image distortions after the measurement. We used a calibration sample, which exhibits periodic surface features with precisely defined distances. For each set of scanning parameters that produce nonlinear distortions, an image of the calibration sample is measured and used to build a displacement tensor. Once a displacement tensor is found for a certain set of scanning parameters, all images that are measured using this set of parameters can be corrected. The advantages of this method are that no additional equipment, except a sample with a periodic pattern, is needed to perform the calibration and that nonlinearities that are not time dependent can be corrected even without knowing their exact origin or quantitative physical description. In addition this method allows us to correct very large nonlinear distortions and to control the aging of the piezotube.

2. Experimental setup and calibration sample

The calibration is illustrated for data acquired using an Omicron VT-STM. The calibration sample is based on a $SrTiO_3$ (Nb doped)

* Corresponding author. Tel.: +49 246 1615 023.
E-mail address: p.ebert@fz-juelich.de (Ph. Ebert).

0304-3991/$ - see front matter © 2013 Elsevier B.V. All rights reserved.
http://dx.doi.org/10.1016/j.ultramic.2013.08.004

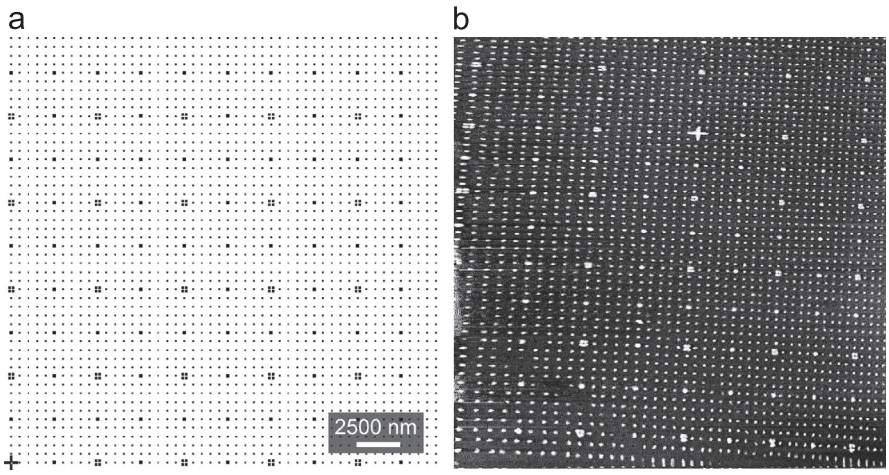

Fig. 1. (a) Schematic view of the dot pattern grown on the $SrTiO_3$ calibration sample. Every fifth and tenth TiO_2 dot is enhanced in size or represented by four closely grouped dots to provide an easy to recognize scale. (b) STM image of the calibration sample. The dot pitch is 500 nm on the entire sample. Note the distinct distortion of the normally regular dot array.

single crystal substrate, which was selected due to its resistance to oxidation or degradation up to very high temperatures, its flatness, and its hardness. The sample was patterned by electron beam lithography. An array of Ti dots with a height of 10 nm and a pitch of 500 nm in both horizontal (x) and vertical (y) directions was deposited using the lift-off technique. The Ti dots were then oxidized to TiO_2 dots. Every fifth and tenth dot is enhanced in size or represented by four closely grouped dots to provide an easy to recognize scale [see Fig. 1(a)]. Ti was chosen as a material for the dots, because Nb-doped $SrTiO_3$, TiO_2 and Ti form electrically conducting contacts with each other.

The electron beam writer (Vistec EBPG 5000plus, positioning accuracy: 5 nm on a $320 \times 320\ \mu m^2$ main field) exhibits very high accuracy of the written pattern. Hence, the error of the dot pitch of $\sim 1\%$ is much smaller than the distortion created by piezo nonlinearities and thus is neglected in the following.

3. Measurement of the distortion

Although the used Omicron VT-STMs exhibit an accurate calibration for atomic scale images, some distortions appear when extending the scan area toward the micrometer range. Fig. 1(b) shows a $15 \times 15\ \mu m^2$ STM image of the calibration sample. Although the dot pitch is 500 nm on the entire sample, the distance between two neighboring dots appears to be larger in the lower left part of the image as compared with the upper right side. The apparent horizontal dot separation in the lower left part of the image is almost reaching twice the apparent dot separation in the upper right part. Also the vertical dot separation is multiplied by a factor of about 1.25 at the lower left side, compared to the upper right.

This distortion does not depend on the scan speed or the movement of the piezotube performed before scanning the image. On the other hand, the size of the scan area and the rotation angle of the scan area do significantly affect the distortions. As an example, Fig. 2 illustrates the distortion of the dot grid as a function of the rotation angle of the scan area. Note the curvature of the rows which depends on the scanning angle. We were able to reproduce this behavior on a 14-year-old Omicron VT-STM as well as on a new one (2010). From these facts we conclude that the commonly known piezocreep and hysteresis as well as piezoelectric aging cannot be the explanation for this distortion alone. There may be some piezocreep or hysteresis resulting from the large deflection of the piezoelectric while scanning micrometer sized images, but due to the very good reproducibility, the most likely explanations for this phenomenon are an inaccurate calibration or linearization of the measurement software at large sized images, a cross coupling between the vertical and horizontal scanning direction, and capacitive coupling of wires and connectors within the STM.

However, sometimes such extreme scanning parameters are needed without changing the internal calibration of a piezoscanner in the SPM measurement software. A good example of the need of acquiring small and large STM images without the possibility to change the software calibration is the imaging of thin films by cross-sectional scanning tunneling microscopy [14–18]. In this case, large areas have to be scanned in order to identify the cross-section of the thin films, followed by nanometer sized images yielding high resolution images of this region.

4. The calibration and rectification algorithm

In a first step, a third order tensor with $m \times n \times 2$ components needs to be created. For the sake of an intuitive understanding and a better distinguishability the third order tensor can be separated into a second order tensor $\underline{\underline{\boldsymbol{P}}}$ where each component is a two-dimensional (2D) vector. This approach is used throughout the following description of the mathematical algorithm.

The second order tensor represents an $m \times n$ grid, which is overlaid with the STM image of the calibration sample. The points of this grid represent the equidistant (undistorted) TiO_2 dots on the calibration sample. Hence, m is the number of dots per column and n is the number of dots per row. Due to the distortion, these numbers are not equal for each column or each row of dots on the STM image. For our purpose, the number of dots per column or row with the fewest dots is usually sufficient. If all points visible at the STM image should be taken into account, the tensors may have some 'empty' components. The dot pitch of the overlaid grid d_x (and d_y) is given by the physical dot pitch $d_{dotpitch,x}$ (and $d_{dotpitch,y}$) of the calibration sample converted into units of pixels:

$$d_x = d_{dotpitch,x} \cdot R_x$$
$$d_y = d_{dotpitch,y} \cdot R_y \quad (1)$$

where the resolution factor R_x (R_y) is defined by

$$R_x = \frac{N_{\mathrm{pixel},x}}{\Delta x_{\mathrm{nominal}}}. \quad (2)$$

$N_{\mathrm{pixel},x}$ is the number of pixels of the STM image in the x direction and $\Delta x_{\mathrm{nominal}}$ represents the nominal scan width in the x direction. R_y follows by analogy.

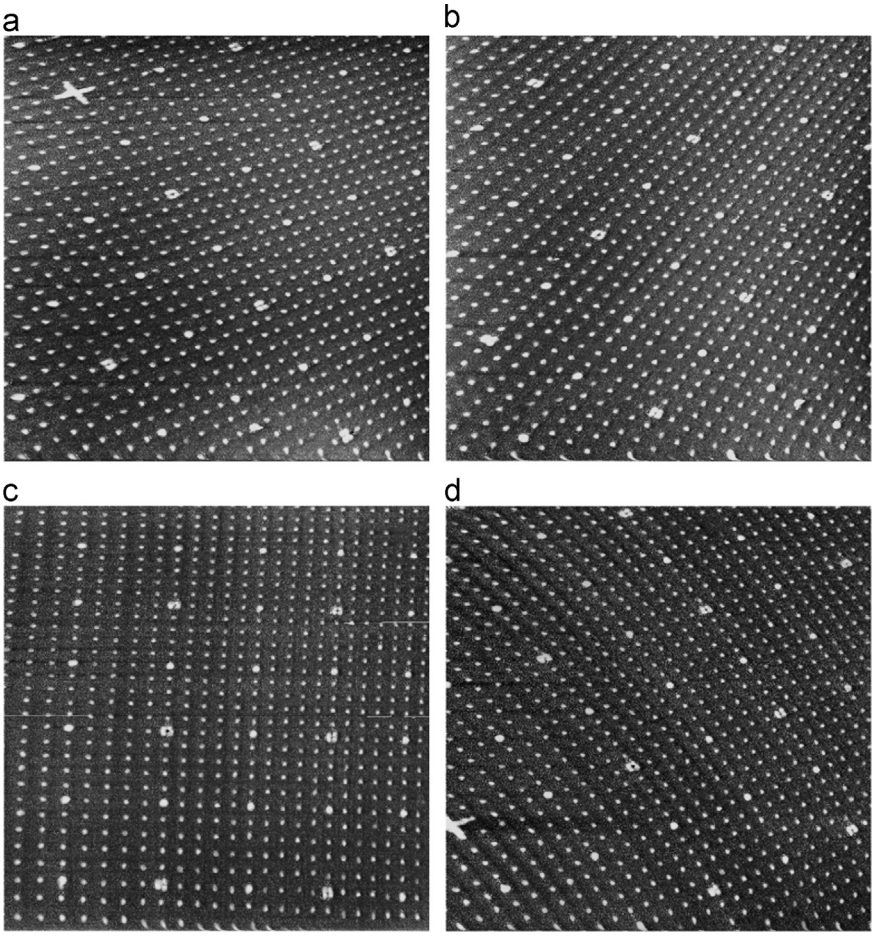

Fig. 2. STM images of the $SrTiO_3$ calibration sample for different scanning directions of (a) 30°, (b) 60°, (c) 90° and (d) 120°. The nominal size of the scan area in all four images is $10 \times 10\ \mu m^2$.

Hence, the components $\boldsymbol{p}_{i,j}$ of the tensor $\underline{\underline{\boldsymbol{P}}}$ representing the points of the grid are given by a 2D position vector:

$$\boldsymbol{p}_{i,j} = \begin{pmatrix} x_0 + j \cdot d_x \cdot \cos(\alpha) - i \cdot d_y \cdot \sin(\alpha) \\ y_0 + j \cdot d_x \cdot \sin(\alpha) + i \cdot d_y \cdot \cos(\alpha) \end{pmatrix}$$

$$\text{with } i = 1 \ldots n,\ j = 1 \ldots m. \tag{3}$$

α denotes the angle between the x-axis and the physical dots along a row. This angle depends on the mounting of the sample on the sample holder relative to the STM scanning direction and hence may not influence the displacement tensor, which describes the distortion and is defined below. Thus the point grid has to be rotated by the same angle. x_0 and y_0 refer to the offset of the grid relative to the underlaying STM image. In order to minimize an undesired deformation of regions of the STM image exhibiting no or only small deviations from the physical dot pitch, x_0 and y_0 have to be chosen such that a maximum number of grid points overlap with their corresponding dots on the underlaying STM image.

In the next step, an $m \times n$ tensor $\underline{\underline{\boldsymbol{A}}}$ of 2D position vectors containing the actually measured (and digitalized) positions of dots on the STM image is created. The units are given in pixels, again. Note that each component $\boldsymbol{a}_{i,j}$ of the tensor $\underline{\underline{\boldsymbol{A}}}$ describes the same TiO_2 dot as $\boldsymbol{p}_{i,j}$, but at another position (x, y) due to the distortion of the image. Hence, the components of $\underline{\underline{\boldsymbol{A}}}$ include the distortion of the dot grid. The goal is to rectify the image in a way, that all components of $\underline{\underline{\boldsymbol{A}}}$ (distorted positions of TiO_2 dots) are moved to their corresponding position in $\underline{\underline{\boldsymbol{P}}}$ (ideal position TiO_2 of dots).

Therefore, the displacement tensor $\underline{\underline{\boldsymbol{M}}}$, where each component $\boldsymbol{m}_{i,j}$ is a 2D displacement vector, can be defined using $\underline{\underline{\boldsymbol{A}}}$ and $\underline{\underline{\boldsymbol{P}}}$:

$$\underline{\underline{\boldsymbol{M}}} = \underline{\underline{\boldsymbol{P}}} - \underline{\underline{\boldsymbol{A}}} \tag{4}$$

Fig. 3(a) shows a visualization of the components of $\underline{\underline{\boldsymbol{M}}}$ (red lines) obtained from the STM image seen in Fig. 1. The original resolution of this STM image is 800×800 px and $\underline{\underline{\boldsymbol{M}}}$ exhibits more than 2500 components. The accuracy of $\underline{\underline{\boldsymbol{M}}}$ and consequently the accuracy of the image correction depend heavily on the number of TiO_2 dots visible in the STM image. As will be discussed later, 2500 dots lead to accurate results for an 800×800 px sized image.

In order to correct a distorted STM image, one has to determine the displacement of each pixel (x, y) of the image. However, since the displacement tensor only contains displacement vectors for $m \times n$ pixels (i.e. the TiO_2 dots) distributed all over the image, the displacement vectors for the remaining pixels need to be interpolated. For achieving this, the distances between a pixel (x, y) and the positions of all of the TiO_2 dots have to be calculated:

$$D(x,y)_{i,j} = \left| \boldsymbol{a}_{i,j} - \begin{pmatrix} x \\ y \end{pmatrix} \right| \tag{5}$$

Subsequently, one has to identify the couples of indices $(i,j)_{k=1\ldots l}$ belonging to the l smallest entries of $D(x,y)$. These are the TiO_2 dots that are located closest to the pixel (x, y). We achieved good results by choosing $l=6$. One is now able to obtain the displacement vector $\boldsymbol{M}(x,y)$ for each pixel (x, y) by calculating the weighted mean of the displacement vectors $\boldsymbol{m}_{i,j}$ belonging to the

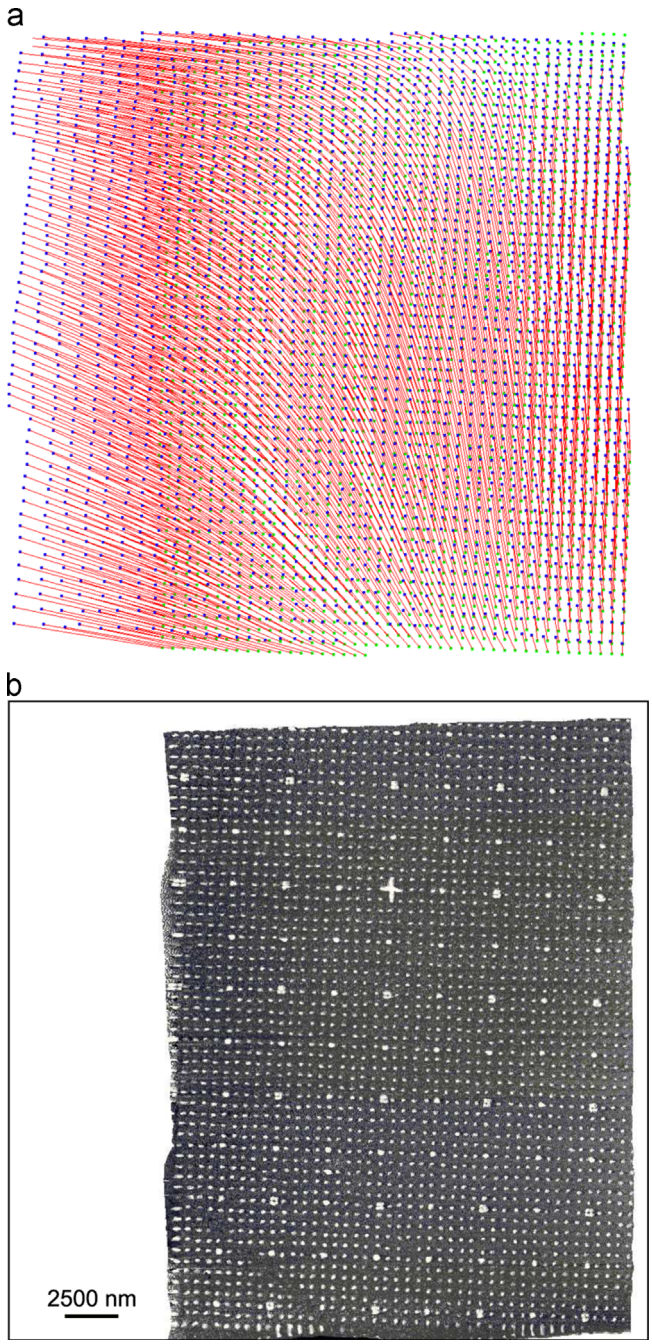

Fig. 3. (a) Visualization of the components $\boldsymbol{m}_{i,j}$ (red) of displacement tensor $\underline{\boldsymbol{M}}$. The vertices correspond to the position vectors $\boldsymbol{p}_{i,j}$ (green) and $\boldsymbol{a}_{i,j}$ (blue). (b) The same STM image as shown in Fig. 1 but with applied distortion correction. (For interpretation of the references to color in this figure caption, the reader is referred to the web version of this article.)

TiO_2 dots that are positioned closest to (x, y):

$$\boldsymbol{M}(x,y) = \frac{1}{\sum_{(i,j)_k}\left(\frac{1}{D'(x,y)_{i,j}}\right)^2}\sum_{(i,j)_k}\left(\frac{1}{D'(x,y)_{i,j}}\right)^2 \cdot \boldsymbol{m}_{i,j} \tag{6}$$

$D'(x,y)_{i,j}$ is defined such that the occurrence of singularities is avoided and the weighting of a displacement vector located at the position (x, y) is maximal:

$$D'(x,y)_{i,j} = \begin{cases} D(x,y)_{i,j} & \text{if } D(x,y)_{i,j} > 0 \\ 1 & \text{else} \end{cases} \tag{7}$$

The resulting displacement vectors for each pixel $\boldsymbol{M}(x,y)$ are used to move all pixels (x, y) of the originally measured STM image to their corrected position (x', y'):

$$\begin{pmatrix} x' \\ y' \end{pmatrix} = \begin{pmatrix} x \\ y \end{pmatrix} + \boldsymbol{M}(x,y) \tag{8}$$

Since the pixel positions have to be integer numbers, rounding errors may arise in the determination of (x', y'). As a result, some pixels of the corrected image may not be assigned to a pixel of the initial image. In order to derive the z value of these unassigned pixels, one has to determine the mean value of their surrounding pixels. Contrariwise, some pixels of the corrected image may be assigned to more than one pixel of the initial image. The z value of these multiple assigned pixels can be obtained by averaging the corresponding pixels of the initial image.

Fig. 3(b) displays the distortion corrected version of Fig. 1(b). The accuracy of the distortion correction can be obtained by comparing the dot separations along the horizontal and vertical directions before and after the correction. As already discussed in Section 3, the horizontal dot separation in the lower left part of Fig. 1(b) is almost twice the separation of the upper right part. Due to the distortion correction, this factor was reduced from 2 to only 1.05 [see Fig. 3(b)]. The equivalent factor for the vertical dot separation was reduced from 1.25 to 1.06. This very good result can be further improved by a decrease of the dot pitch of the calibration sample on the one hand and by some additional modifications of the displacement tensor, as described below, on the other hand.

Since the image distortion depends on the set of scanning parameters, the displacement tensor also does. Thus, each set of scanning parameters requires an appropriate displacement tensor.

Finally, it is recommended to reperform this calibration once in a while, especially after the bake out in order to control the aging and degradation of the piezotube.

5. Discussion of remaining distortions

Fig. 3(b) shows that the correction process provides good results for most of the surface area. Only at the left edge of the corrected image the dot spacing is still too large, i.e. it is under corrected. In addition, the outermost dot column at the left edge exhibits some kind of curvature after the correction. These effects arise from the correction algorithm: if the displacement vectors in $\underline{\boldsymbol{M}}$ increase (decrease) strongly by approaching the edge of the STM image, the distortion is under (over) corrected at the outermost edge. This is a consequence of the fact that the pixels in this region are not surrounded by displacement vectors anymore. Therefore, only displacement vectors located right to the left edge of the image can be accounted by Eq. (6). Hence, in our case, the derived displacement vectors for each pixel $\boldsymbol{M}(x,y)$ will be too small at the left edge yielding the observed under correction. In analogy, the curvature and offsets of the left edge arise from the occurrence of an additional dot column at the upper left edge of the STM image. Due to the additional dots, a better correction is provided for the uppermost left area. This problem may be reduced by extrapolating the distortion over the image edge. However, the difficulty of this approach lies in the fact that the results depend on the exact extrapolation model.

Another effect is related to the interpolation of the displacement vectors for pixels in between the TiO_2 dots. If the displacement vectors of neighboring dots change their direction strongly from one dot to the next (e.g. due to noise in the STM image), the displacement vectors $\boldsymbol{M}(x,y)$ of the individual pixels in between the dots will exhibit sudden alternations, whenever the averaging according to Eq. (6) moves from one set $(i,j)_{k=1\ldots l}$ of l TiO_2 dots to

another set of l dots. This problem can be reduced by averaging the displacement vectors $\boldsymbol{M}(x,y)$ of several STM images of the calibration sample acquired with the same parameters. Another possibility is the smoothing of $\boldsymbol{M}(x,y)$ by a median- or gauss-filter. The application of filters improves the smoothness of the distortion corrected image, but the drawback is a loss of accuracy of the distortion correction: a dot at the location $\boldsymbol{a}_{i,j}$ is not exactly moved to the predetermined position $\boldsymbol{p}_{i,j}$, anymore. Thus, the application of smoothing filters should be kept to a minimum, while the TiO_2 dot pitch and hence the number of components of $\underline{\underline{\boldsymbol{M}}}$ should be maximized.

6. Conclusion

In conclusion, we illustrated a methodology to correct distortions in SPM images without the need of additional instrumentation, like optical or capacitive tracking systems. By employing a $SrTiO_3$ sample with an evenly distributed TiO_2 dot grid, reproducible image distortions could be observed and corrected, even without detailed knowledge about the physical origin of the nonlinear behavior of the piezoelectric scanning tube. In our example, the apparent dot separation between two different parts of the measured STM image on the calibration sample differed by up to a factor of 2. By applying the correction algorithm, this factor was reduced to approximately 1.05.

Acknowledgments

The authors thank S. Trellenkamp, R. Borowski, and L. Jin for their assistance with the sample preparation, M. Moors for allowing us to measure the calibration sample at a new Omicron VT-STM, and the DFG for financial support under Grant no. Eb 197/5-1.

References

[1] J. William, N. Sharpe, Springer Handbook of Experimental Solid Mechanics, Springer Science+Business Media LLC, New York, 2008.
[2] G. Binnig, D.P.E. Smith, Review of Scientific Instruments 57 (1986) 1688 http://dx.doi.org/10.1063/1.1139196.
[3] P. Ge, M. Jouaneh, Precision Engineering 17 (1995) 11.
[4] R. Barrett, C. Quate, Review of Scientific Instruments 62 (1991) 1393 http://dx.doi.org/10.1063/1.1142506.
[5] S. Gonda, T. Doi, T. Kurosawa, Y. Tanimura, N. Hisata, T. Yamagishi, H. Fujimoto, H. Yukawa, Applied Surface Science 144–145 (1999) 505, http://dx.doi.org/10.1016/S0169-4332(98)00851-4.
[6] S. Gonda, T. Doi, T. Kurosawa, Y. Tanimura, Review of Scientific Instruments 70 (1999) 3362.
[7] H.-U. Danzebrink, L. Koenders, G. Wilkening, A. Yacoot, H. Kunzmann, CIRP Annals – Manufacturing Technology 55 (2006) 841, http://dx.doi.org/10.1016/j.cirp.2006.10.010.
[8] J.A. Miller, R. Hocken, S.T. Smith, S. Harb, Precision Engineering 18 (1996) 95, http://dx.doi.org/10.1016/0141-6359(96)00037-2.
[9] H. Sawano, T. Gokan, H. Yoshioka, H. Shinno, Precision Engineering 36 (2012) 538, http://dx.doi.org/10.1016/j.precisioneng.2012.02.007.
[10] A.E. Holman, C.D. Laman, P.M.L.O. Scholte, W.C. Heerens, F. Tuinstra, Review of Scientific Instruments 67 (1996) 2274.
[11] G. Picotto, S. Desogus, S. Lanyi, R. Nerino, A. Sosso, Journal of Vacuum Science & Technology B 14 (1996) 897.
[12] F. Meli, R. Thalmann, Measurement Science & Technology 9 (1998) 1087 http://dx.doi.org/10.1088/0957-0233/9/7/014.
[13] F. Hüe, C.L. Johnson, S. Lartigue-Korinek, G. Wang, P.R. Buseck, M.J. Hÿtch, Journal of Electron Microscopy 54 (2005) 181, http://dx.doi.org/10.1093/jmicro/dfi042.
[14] W. Barvosa-Carter, M.E. Twigg, M.J. Yang, L.J. Whitman, Physical Review B 63 (2001) 245311.
[15] H. Chen, R.M. Feenstra, R.S. Goldman, C. Silfvenius, G. Landgren, Applied Physics Letters 72 (1998) 1727.
[16] R.M. Feenstra, D.A. Collins, D.Z.-Y. Ting, M.W. Wang, T.C. McGill, Journal of Vacuum Science & Technology B 12 (1994) 2592.
[17] M. Pfister, M.B. Johnson, S.F. Alvarado, H.W.M. Salemink, U. Marti, D. Martin, F. Morier-Genoud, F.K. Reinhart, Applied Physics Letters 65 (1994) 1168.
[18] F. Marczinowski, J. Wiebe, J.M. Tang, M.E. Flatté, F. Meier, M. Morgenstern, R. Wiesendanger, Physical Review Letters 99 (2007) 157202.